**ARTICLE**

Constructed Mott–Schottky Heterostructure Catalyst to Trigger Interface Disturbance and Manipulate Redox Kinetics in Li-O$_2$ Battery

Yongji Xia[1], Le Wang[1], Guiyang Gao[1], Tianle Mao[1], Zhenjia Wang[1], Xuefeng Jin[1], Zheyu Hong[1], Jiajia Han[1] ✉, Dong-Liang Peng[1] ✉, Guanghui Yue[1] ✉

HIGHLIGHTS

- A carbon free self supported Mott-Schottky heterostructure was constructed as an efficient cathode catalyst for lithium oxygen batteries, achieving homogeneous contact between the two materials for strong interfacial interactions.

- The heterostructure triggered interfacial perturbations and band structure changes, which accelerated oxygen reduction reaction (ORR) and oxygen evolution reaction (OER) kinetics, resulting in an extremely long cycle life of 800 cycles and an extremely low overpotential of 0.73 V.

- Combined with advanced characterization techniques and density functional theory calculations, the underlying mechanism behind the boosted ORR/OER activities and the electrocatalytic mechanism were revealed.

ABSTRACT Lithium-oxygen batteries (LOBs) with high energy density are a promising advanced energy storage technology. However, the slow cathodic redox kinetics during cycling causes the discharge products to fail to decompose in time, resulting in large polarization and battery failure in a short time. Therefore, a self-supporting interconnected nanosheet array network NiCo$_2$O$_4$/MnO$_2$ with a Mott–Schottky heterostructure on titanium paper (TP-NCO/MO) is ingeniously designed as an efficient cathode catalyst material for LOBs. This heterostructure can accelerate electron transfer and influence the charge transfer process during adsorption of intermediate by triggering the interface disturbance at the heterogeneous interface, thus accelerating oxygen reduction and oxygen evolution kinetics and regulating

product decomposition, which is expected to solve the above problems. The meticulously designed unique structural advantages enable the TP-NCO/MO cathode catalyst to exhibit an astounding ultra-long cycle life of 800 cycles and an extraordinarily low overpotential of 0.73 V. This study utilizes a simple method to cleverly regulate the morphology of the discharge products by constructing a Mott–Schottky heterostructure, providing important reference for the design of efficient catalysts aimed at optimizing the adsorption of reaction intermediates.
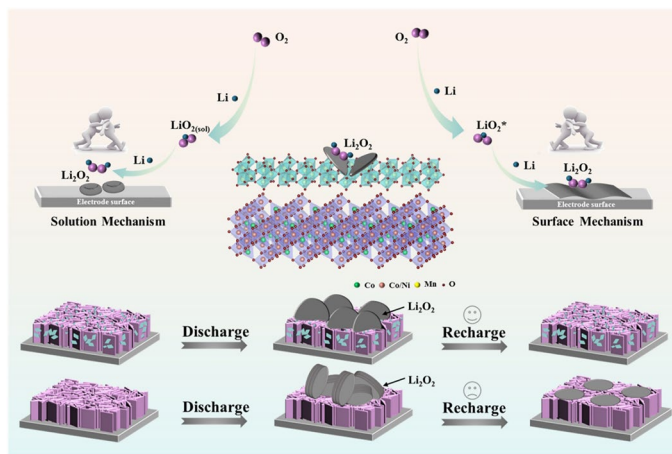
KEYWORDS Mott–Schottky heterostructure; Lithium-oxygen batteries; Electrocatalysts; Electrodeposition

✉ Jiajia Han, jiajiahan@xmu.edu.cn; Dong-Liang Peng, dlpeng@xmu.edu.cn; Guanghui Yue, yuegh@xmu.edu.cn
[1] State Key Lab of Physical Chemistry of Solid Surface, Fujian Key Laboratory of Surface and Interface Engineering for High Performance Materials, College of Materials, Xiamen University, Xiamen 361005, People's Republic of China

1 Introduction

Lithium-oxygen batteries (LOBs) are capable of delivering ultra-high energy density and are expected to fulfill the growing demand for high-energy–density devices in future [1–3]. Non-aqueous LOBs [4, 5] face bottlenecks such as poor rate performance, low practical capacity and short cycle life [6–8] due to the slow three-phase (gas/solid/liquid) reaction, the stacking of the insulated discharge product on the cathode side, as well as parasitic reactions caused by attacks from superoxide radicals and singlet oxygen ($^1O_2$) in the electrolyte [1, 4, 9–11]. Among them, the adsorption and morphology of the discharge products/intermediates at the cathode side are important factors affecting the above issues [12]. The adsorption capacity of the reaction intermediates is inextricably linked to the overpotential, the cycling reversibility, and the capacity [13–15]. Therefore, finding effective strategies to regulate the adsorption of discharge products/intermediates is the ultimate goal of designing efficient electrocatalysts.

Designing multiphase interfaces and regulating the active site distribution of electrocatalysts may be an effective strategy to induce transformative changes in oxygen reduction (ORR) and oxygen evolution (OER) activity and intermediate sorption energy. When two materials with different work functions contact each other, electron redistribution will occur at the heterogeneous interface to adjust the Fermi level of adjacent components, known as the Mott–Schottky effect [16], to establish a robust built-in electric field [17] to promote electron transfer. The heterogeneous interface will alter the work function and electron cloud density of the material, enhancing the adsorption of oxygen and desorption the products. The Mott–Schottky heterostructures have been used as a catalyst for lithium-sulfur batteries and Li-CO$_2$ batteries and have demonstrated excellent catalytic activity [16, 18–23]. In addition, the interface disturbance caused by the heterostructure can effectively change the charge distribution of the active site [24, 25], thus regulating the morphology of Li$_2$O$_2$ [26]. For example, Yin et al. [27] designed a NiCo$_2$S$_4$/NiO heterostructure cathode catalyst in which the discharge product Li$_2$O$_2$ grows into a large size pea-like shape, endowing the electrode with an extremely high discharge capacity of up to 10,050 mAh g^{-1} and a tiny overpotential of 0.88 V. Similarly, Yan et al. designed a hierarchical heterostructure MnO$_2$-Co$_3$O$_4$ to achieve embedded

growth of bulk Li$_2$O$_2$ [28]. The embedded large mooncake and flake Li$_2$O$_2$ provide enhanced cycle stability, excellent rate performance and high capacity. Therefore, it is feasible to carefully select appropriate materials to construct reasonable heterogeneous structures to regulate work functions and achieve high performance LOBs. However, achieving uniform contact between the two materials to obtain strong interfacial interactions is a challenge, which to some extent limits the capacity and battery life of LOBs. Furthermore, there is a lack of studies on the heterogeneous structure and intermediate adsorption behavior, as well as the distribution and formation mechanism of discharge products.
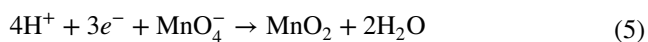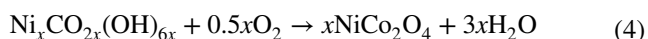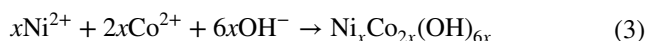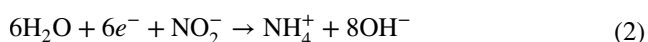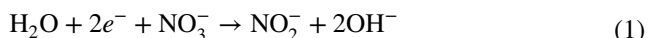
In this work, a facile electrodeposition combined with hydrothermal method was employed to achieve the growth of uniform vertically interconnected arrays of NiCo$_2$O$_4$ nanosheets attached with small flakes of MnO$_2$ on the surface of smooth titanium paper (TP-NCO/MO). The design of self-supporting structures suppresses the aggregation of catalyst materials, enabling uniform contact between the two materials and exposing more catalytic active sites. Electron energy loss spectroscopy (EELS) and other characterization confirm that the construction of NiCo$_2$O$_4$/MnO$_2$ heterostructure triggers the interface disturbance at the heterogeneous interface and induces the interface charge reconstruction, thus adjusting the adsorption energy of the intermediate and promoting the product decomposition. Density functional theory (DFT) calculations demonstrate that LiO$_2$ adsorbs weakly on NiCo$_2$O$_4$/MnO$_2$. The weak adsorption of the intermediate product LiO$_2$ within an optimal range facilitates the swift conversion of the intermediate to the final product, accelerating the kinetics of discharge product formation. Ultimately, the LOB assembled with TP-NCO/MO cathode exhibited over 800 cycles of cycling performance, low overpotential of 0.73 V and excellent rate capability. A series of characterizations revealed that the discharge products in the TP-NCO/MO electrode had high reversibility. These results serve as a valuable guide for creating efficient LOBs catalysts.

2 Experimental Section

2.1 Preparation of TP-NCO/MO

A facile electrodeposition was adopted to prepare NiCo$_2$O$_4$ nanosheets on TP. Before deposition, TP was first soaked

in HNO_3 for 8 h to clean the surface and remove the oxide layer. The solution of 0.3 M $Co(NO_3)_2 \cdot 6H_2O$ and 0.15 M $Ni(NO_3)_2 \cdot 6H_2O$ was synthesized as the electrolyte, while Pt sheet and 4×4 cm^2 TP were utilized as counter/reference electrode and working electrode, respectively. An electrochemical station was utilized to apply a constant current of 10 mA cm^{-2} for 15 min. After deposition, samples were washed with DI water and ethanol and then held in muffle furnace at 300 °C for 3 h to obtain the TP-NCO. The as-prepared TP-NCO was placed in 70 mL aqueous solution containing 0.1106 g $KMnO_4$ and 40 μL H_2SO_4 and maintained at 80 °C for 1 h to perform hydrothermal reaction. After washing, the sample was calcined at 400 °C in the air for 4 h. The catalyst TP-NCO/MO was obtained after cooling to room temperature. The chemical reaction equations involved are as follows:

$$H_2O + 2e^- + NO_3^- \rightarrow NO_2^- + 2OH^- \tag{1}$$

$$6H_2O + 6e^- + NO_2^- \rightarrow NH_4^+ + 8OH^- \tag{2}$$

$$x\mathrm{Ni}^{2+} + 2x\mathrm{Co}^{2+} + 6x\mathrm{OH}^- \rightarrow \mathrm{Ni}_x\mathrm{Co}_{2x}(\mathrm{OH})_{6x} \tag{3}$$

$$\mathrm{Ni}_x\mathrm{CO}_{2x}(\mathrm{OH})_{6x} + 0.5x\mathrm{O}_2 \rightarrow x\mathrm{NiCo}_2\mathrm{O}_4 + 3x\mathrm{H}_2\mathrm{O} \tag{4}$$

$$4H^+ + 3e^- + MnO_4^- \rightarrow MnO_2 + 2H_2O \tag{5}$$

2.2 Material Characterization

The phase structure of catalyst materials was determined by X-ray diffraction (XRD, Bruker AXS) with Cu-kα radiation at 40 kV and 40 mA. The surface morphology and microstructure of the materials were observed using scanning electron microscopy (SEM, SU70, Hitachi) and transmission electron microscopy (TEM, TECNAI F-30). Electron energy loss spectroscopy (EELS) was performed by JEOL JEM-F200 (operating voltage 200 kV). Raman spectra were recorded by a HR Evolution high-resolution confocal laser Raman system (France, Horiba FRANCE SAS) with a wavelength of 532 nm. N_2 adsorption/desorption analysis curves were obtained by a 3H-2000PM2 analyzer. The specific surface area and pore size distribution curves of the material were obtained using the BJH model. The X-ray photoelectron spectroscopy (XPS) were recorded on Thermo Scientific K-Alpha spectrometer (USA). FTIR spectroscopy was measured on a Fourier infrared spectrometer (Nicolet IS50). UV–vis diffuse reflectance spectroscopy was obtained with Shimadzu UV-3600i Plus of Japan. TOF–SIMS was performed on an IONTOF M6, and in situ EIS was carried out on a PARSTAT 3000A-DX electrochemical workstation (AMETEK Instrument Co., Ltd.).

2.3 Electrochemical Measurements

The prepared TP-NCO/MO and TP-NCO were cut into electrodes with a diameter of 12 mm, which were directly used as the cathode of LOBs. Lithium foil with a thickness of 0.6 mm was used as a counter electrode, and glass fiber (Whatman, GF/D) was used as the diaphragm, the electrolyte was 1 M LiTFSI in TEGDME (Canrd Technology Co., Ltd.). The 2032 battery was assembled in the Ar atmosphere glove box and was transferred to the glass test bottle filled with O_2 for battery testing after a period of standing. The constant current charge and discharge tests were conducted on a NEWARE BTS multi-channel battery system (Shenzhen, China) with a voltage range set at $2.0 - 4.8$ V (vs Li$^+$/Li). The MnO_2 and Super P oxygen cathodes were obtained by mixing and stirring the catalyst material (MnO_2 /Super P): CNT: polyvinylidene fluoride (PVDF) at a ratio of 4:4:2 and coated on a 12 mm carbon paper. The rest is the same as the above process. Cyclic voltammetry (CV) and electrochemical impedance spectroscopy (EIS) were recorded by CHI660D electrochemical workstation. CV was performed at a sweep rate of 0.1 mV s^{-1} in the voltage range of 2.0–4.5 V (vs Li$^+$/Li), and EIS testing was performed in the frequency range of 10^5 to 0.01 Hz and a sine wave of 5 mV. The band edge potential of the catalysts was measured by the Mott–Schottky test using a Pt counter electrode, an Ag/AgCl reference electrode and a catalyst working electrode in 0.5 M Na_2SO_4 solution at a frequency of 2000 Hz.

2.4 DFT Calculations

Vienna Ab initio Simulation Package (VASP) was used to perform the first-principles calculation, using the projector-augmented wave method based on DFT [29]. The generalized gradient approximation (GGA) of the Perdew–Burke–Ernzerhof (PBE) exchange–correlation functional was selected for calculation [30]. The correction of

van der Waals interaction adopted the Grimme DFT-D3 method [31]. A plane-wave (PW) cutoff energy of 500 eV was set. The relaxation and self-consistent calculation were based on the $3 \times 3 \times 1$ k-point mesh generated by the Monkhorst–Pack (M–K) scheme. The convergence criteria are 1×10^{-5} eV energy differences for solving the electronic wave function, and the structures were relaxed until the forces on all atoms were smaller than -0.02 eV Å^{-1}, while the perovskite lattice parameters and the bottom two-layer atoms were fixed. A vacuum layer over 15 Å along the z-direction was provided to eliminate direct interaction between adjacent plates. A post-stage van der Waals DFT-D3 method with Becke-Johnson damping was applied [31], and the Hubbard-U corrections to the d-electrons of Ru and Ir following the approach proposed by Dudarev et al. [32] were considered. The values of the effective Hubbard-U parameter U = 3.3, 3.9, and 6.2 eV are chosen for Co, Mn, and Ni, respectively, determined by linear response approach [33].
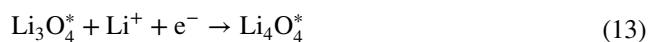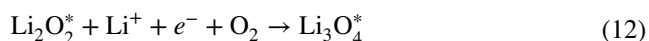
In practice, $NiCo_2O_4$ on MnO_2 may exist in a variety of crystalline surface combinations. We found that the low-index facet of $NiCo_2O_4$ has a good matching with MnO_2, and the interfacial strain is lower than 1.5%, from which MnO_2 can be easily epitaxial grown on this crystalline facet. We adopt this model as the mechanism study in the calculation.

The possible reaction paths of Li^+ and O_2 on the surface of $NiCo_2O_4/MnO_2$:

$4e^-$ pathway:

$$Li^+ + e^- + O_2 \rightarrow LiO_2^* \tag{6}$$

$$LiO_2^* + Li^+ + e^- \rightarrow Li_2O_2^* \tag{7}$$

$$Li_2O_2^* + Li^+ + e^- \rightarrow Li_3O_2^* \tag{8}$$

$$Li_3O_2^* + Li^+ + e^- \rightarrow Li_4O_2^* \tag{9}$$

$2e^-$ pathway:

$$Li^+ + e^- + O_2 \rightarrow LiO_2^* \tag{10}$$

$$LiO_2^* + Li^+ + e^- \rightarrow Li_2O_2^* \tag{11}$$

$$Li_2O_2^* + Li^+ + e^- + O_2 \rightarrow Li_3O_4^* \tag{12}$$

$$Li_3O_4^* + Li^+ + e^- \rightarrow Li_4O_4^* \tag{13}$$

3 Results and Discussion

3.1 Synthesis and Characterization of Catalysts

Figure 1a outlines the preparation process of TP-NCO/MO. Initially, the precursor nanosheet arrays were vertically and uniformly deposited on the surface of titanium fiber using a facile electrodeposition technique. During this process, oxynitrate anions on the cathode side were reduced to form hydroxide. The synthesized metal hydroxide precursor was calcined in air to obtain $NiCo_2O_4$. Subsequently, small MnO_2 flakes were grown on the surface of $NiCo_2O_4$ nanosheets through hydrothermal and calcination processes. SEM images were obtained to reveal the surface morphology of the materials. The comparative views of the TP-NCO and TP-NCO/MO nanosheet arrays are clearly shown in Fig. 1b, c. Notably, small and thin flakes of MnO_2 nanosheets grow on the surface of TP-NCO/MO nanosheets, while the surface of TP-NCO nanosheets appears smooth. The presence of MnO_2 flakes does not block the original pore channels, as evidenced by the cross-sectional SEM image of TP-NCO/MO in Fig. 1d. Figure 1d also shows that the nanosheet arrays are arranged vertically aligned on the substrate and are tightly connected to the substrate without obvious gaps. Rough measurements indicate that the thickness of the TP-NCO/MO nanosheet array is approximately 3.47 μm. The elemental mapping images in Fig. S7 illustrate that the Co, Ni, Mn, and O elements are uniformly distributed across the titanium fiber. The presence of MnO_2 can be demonstrated by TEM. The morphology of NCO/MO nanosheet arrays scraped from TP is shown in Fig. 1e. It can be seen that the nanosheet arrays are transparent, indicating their ultra-thin characteristics and the existence of inter-nanosheet channels, which aligns with the conclusions drawn from SEM. The high-resolution TEM (HRTEM) image demonstrates a distinct heterogeneous interface in the material (Fig. 1f). The lattice stripes, with a lattice spacing of 0.470 and 0.244 nm below the interface, correlate to the (111) and (311) crystal planes of $NiCo_2O_4$, respectively. The lattice fringes above
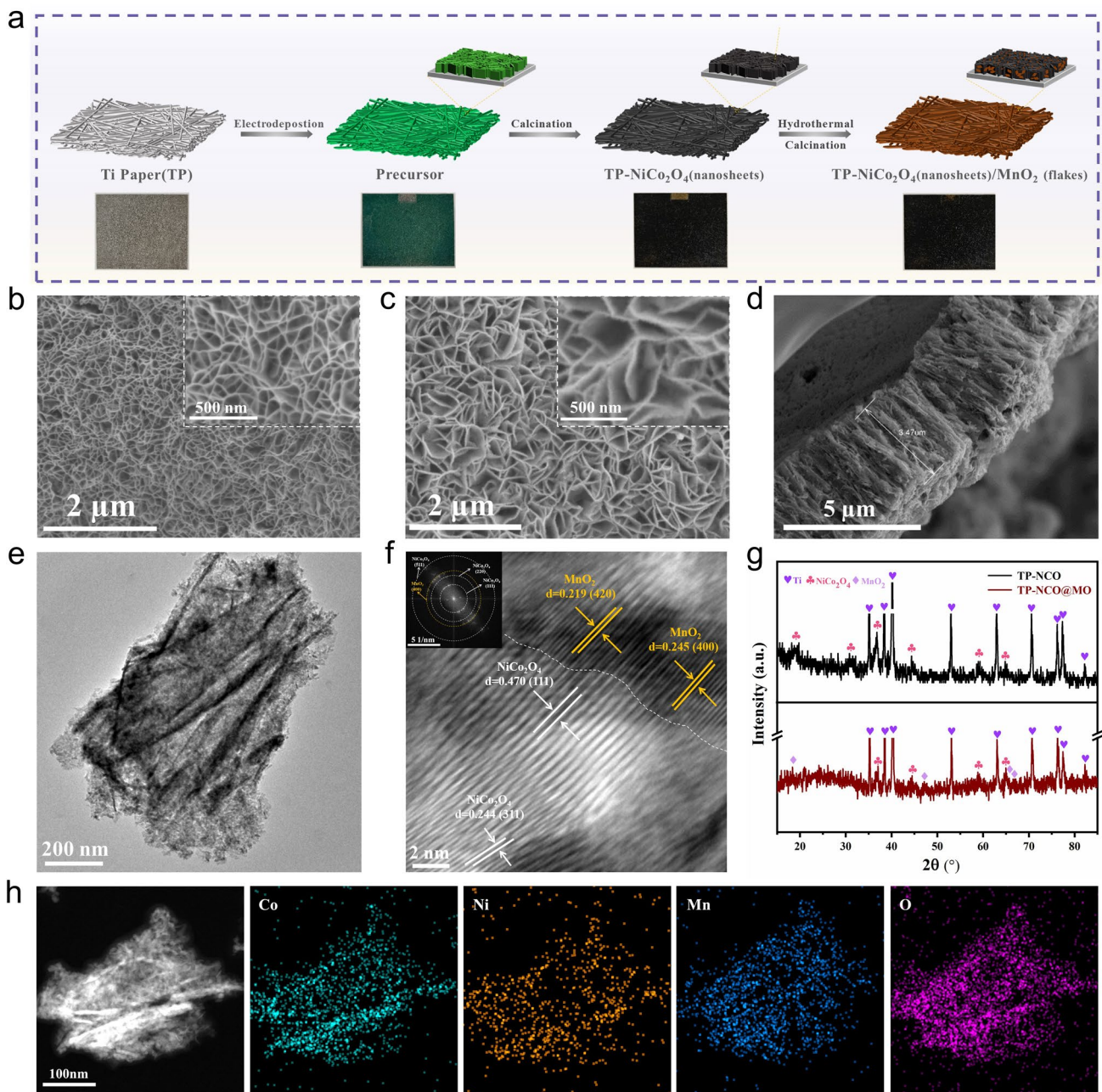
Fig. 1 **a** Flow illustration of TP-NCO/MO preparation. SEM pattern of **b** TP-NCO and **c** TP-NCO/MO array (inset shows its further enlargement). **d** Cross-sectional SEM image of TP-NCO/MO. **e** TEM pattern of NCO/MO array. **f** HRTEM pattern of NCO/MO. (inset shows the corresponding FFT pattern) **g** XRD patterns of TP-NCO/MO and TP-NCO. **h** Elemental mapping of NCO/MO

the interface correspond to the (420) and (400) crystal planes of MnO_2, respectively. The HRTEM conclusion is supported by the corresponding fast Fourier transform (FFT) results in the illustration. The results further confirm that MnO_2 was successfully grown on the surface of $NiCo_2O_4$ nanosheets, forming a close contact to create

a heterogeneous interface. The elemental distribution on the side of the nanosheets array was revealed by the high-angle annular dark-field scanning TEM (HAADF-STEM) and corresponding elemental mappings in Fig. 1h. The image showed that Co and Ni elements were more concentrated in the branches of the nanosheet. These findings

were consistent with the SEM results, indicating the growth of MnO_2 on the surface of $NiCo_2O_4$ nanosheets. The phases of TP-NCO/MO and TP-NCO were further characterized by XRD tests (Fig. 1g). The pronounced diffraction peaks in TP-NCO can be indexed to the substrate Ti (JCPDS No. 65–3362) and spinel-type $NiCo_2O_4$, respectively. The intense diffraction peaks of Ti cover the peaks of other phases to a certain extent, so they were treated as breakpoints. Specifically, the diffraction peaks situated at 18.9°, 31.1°, 36.7°, 44.6°, 59.1°, and 65.0° can be retrieved as the (111), (220), (311), (400), (511), and

(440) crystal planes of $NiCo_2O_4$ (JCPDS No. 20–0781), respectively. For TP-NCO/MO, except for the diffraction peaks associated with Ti and $NiCo_2O_4$, the diffraction peaks at 36.7°, 37.5°, 47.4°, 60.3°, and 65.1° correspond to the (400), (211), (510), (521), and (002) crystal planes of α-MnO_2 (JCPDS No. 44–0141), respectively, where the diffraction peaks at 36.7° and 65.1° basically coincide with $NiCo_2O_4$. The Raman results can further confirm the presence of $NiCo_2O_4$ and MnO_2 in the catalyst material (Fig. S10). According to literature reports, MnO_2 has a variety of crystal structures, such as α-MnO_2, β-MnO_2 γ-MnO_2,
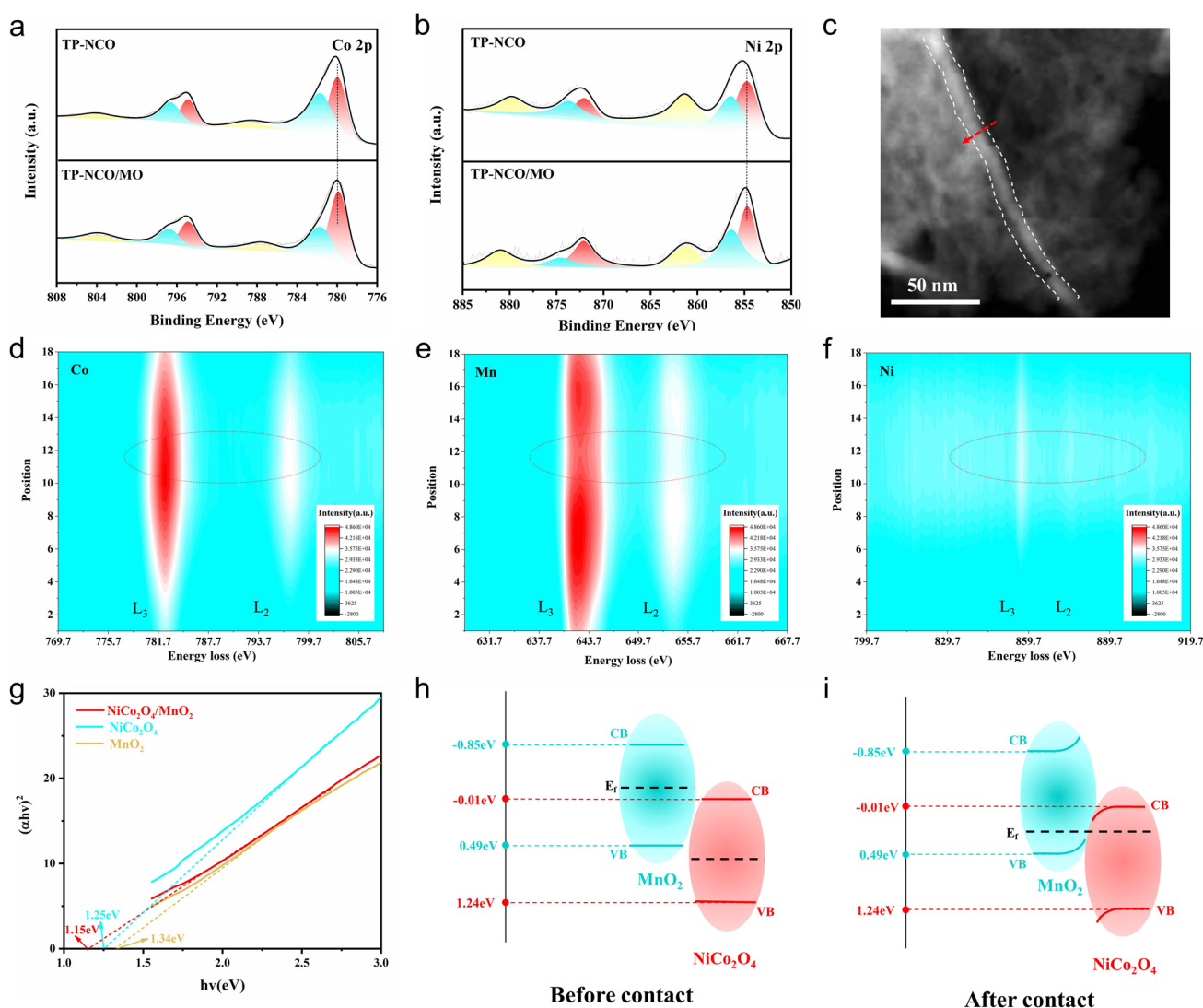

Fig. 2 High-resolution XPS spectrum of **a** Co 2*p* and **b** Ni 2*p* of TP-NCO/MO and TP-NCO. **c** STEM image and EELS scanning direction (red arrow). EELS spectra of **d** Co $L_{2,3}$-edges, **e** Mn $L_{2,3}$-edges and **f** Ni $L_{2,3}$-edges. **g** Bandgap of the $NiCo_2O_4$/MnO_2, $NiCo_2O_4$ and MnO_2 calculated from the plots of $(\alpha h\nu)^2$. versus the photon energy (hν). Possible energy band diagrams of **h** before contact and **i** after contact for $NiCo_2O_4$ and MnO_2

δ-MnO_2, and ε-MnO_2 [34–38]. Among them, the essential structural unit of α-MnO_2 consists of [MnO_6] octahedral double chains, which are intertwined in the plane with adjacent double chains to form a $(2 \times 2) + (1 \times 1)$ tunnel structure [39]. The tunnel structure can promote the transport of discharge products, Li^+ and O_2, improve the formation and breakdown efficiency of discharge products, and degrade overpotential.

3.2 Exploration of Heterogeneous Interfaces

XPS was utilized to acquire the information on possible electronic structure alterations, elemental composition and chemical environment of the catalyst materials. The full spectrum of TP-NCO/MO shows the presence of Co, Ni, O, and Mn signals (Fig. S11a), with the elemental contents of 5.96%, 2.92%, 64.47%, and 26.65%, respectively (Fig. S12), and the ratio of Co and Ni elementals is close to 2:1, which is consistent with the expected results. Figure 2a shows the high-resolution fine spectra of TP-NCO@MO and TP-NCO on Co 2p. For TP-NCO@MO, the characteristic peaks at 779.75 and 794.86 eV link to Co^{3+} 2$p_{3/2}$ and Co^{3+} 2$p_{1/2}$, whereas the peaks at 781.65 and 796.75 eV are associated with Co^{2+} 2$p_{3/2}$ and Co^{2+} 2$p_{1/2}$, 787.53 and 803.82 eV are considered satellite peaks. In contrast to TP-NCO, TP-NCO@MO has a slight displacement toward low binding energy. Regarding the high-resolution spectrum for Ni 2p (Fig. 2b), in TP-NCO@MO, the peaks at 854.69 and 872.13 eV belong to Ni^{2+} 2$p_{3/2}$ and Ni^{2+} 2$p_{1/2}$, 856.37 and 874.58 eV correspond to Ni^{3+} 2$p_{3/2}$ and Ni^{3+} 2$p_{1/2}$, 861.25 and 881.01 eV are considered satellite peaks. Compared with TP-NCO, Co 2p and Ni 2p are negatively shifted in TP-NCO@MO, which suggests that the presence of MnO_2 induces a change in the bonding environment [40], indicating a strong electronic interaction between $NiCo_2O_4$ and MnO_2, which is an electronic coupling effect induced by the establishment of a heterogeneous interface. Reasonable regulation of the electronic structure of the catalyst can optimize its adsorption capacity for oxygen-containing intermediates, which is crucial for enhancing the catalytic performance of electrocatalysts [41]. EELS was used to analyze the local electronic interactions near the NCO/MO interface. Figure S13 displays the distribution of elements in the material. The results show that the lighter regions in Fig. 2c are concentrated with Co and Ni elements, which are identified as $NiCo_2O_4$, while MnO_2 is distributed around them, which is consistent with the mapping results in Fig. 1h. The EELS scanning direction (red arrow in Fig. 2c) moves from MnO_2 to $NiCo_2O_4$ and back to MnO_2, and there are significant intensity changes and slight peak shifts on the Co L_3 and Mn L_3 edges, indicating strong electron interactions within the region [42, 43]. When $NiCo_2O_4$ and MnO_2 are coupled to form a heterogeneous interface, the electronic structure of Co, Ni and Mn atoms is affected, which is manifested as the changes in the peak strength and positions of $L_{2,3}$-edges on both sides of the interface (Fig. 2d-f). The results are consistent with the above XPS conclusions. According to the Mott–Schottky (M-S) analysis (Fig. S14) and UV–vis diffuse reflectance spectroscopy (Figs. S15 and 2 g), the possible energy band diagrams of $NiCo_2O_4$/MnO_2, $NiCo_2O_4$, and MnO_2 are displayed in Fig. 2h, i. Upon the construction of the $NiCo_2O_4$/MnO_2 Mott–Schottky heterostructure, the electron interactions at the interface will spontaneously adjust the Fermi energy levels on both sides of the interface to reach an equilibrium state, which facilitates the charge transfer and alters the underlying reaction process, ultimately enhancing the catalytic activity of the material. The above results provide strong evidence for the successful construction of a heterogeneous interface between $NiCo_2O_4$ and MnO_2.

3.3 Analysis of Electrochemical Performances

To evaluate the electrocatalytic feasibility of TP-NCO/MO material, we directly used it as a free-standing air cathode for discharge and charge tests. Figure 3a displays the cyclic voltammetry (CV) curves of TP-NCO/MO and TP-NCO cathode materials in the voltage range of 2.0–4.5 V (vs. Li/Li^+). The results show that the TP-NCO/MO cathode exhibits higher current density during the ORR/OER process and possesses more pronounced oxidation and reduction peaks [44, 45]. To evaluate the rate performance of TP-NCO/MO and TP-NCO catalyst materials, the current density was progressively raised from 0.1 to 1 mA cm^{-2} and then gradually lowered to 0.1 mA cm^{-2} under the limiting capacity of 0.5 mAh cm^{-2} (Fig. 3b). For TP-NCO/MO, the charging voltage only increases by only 0.05 V and the discharge termination voltage decreases by 0.13 V when the current density returns to 0.1 mA cm^{-2}.
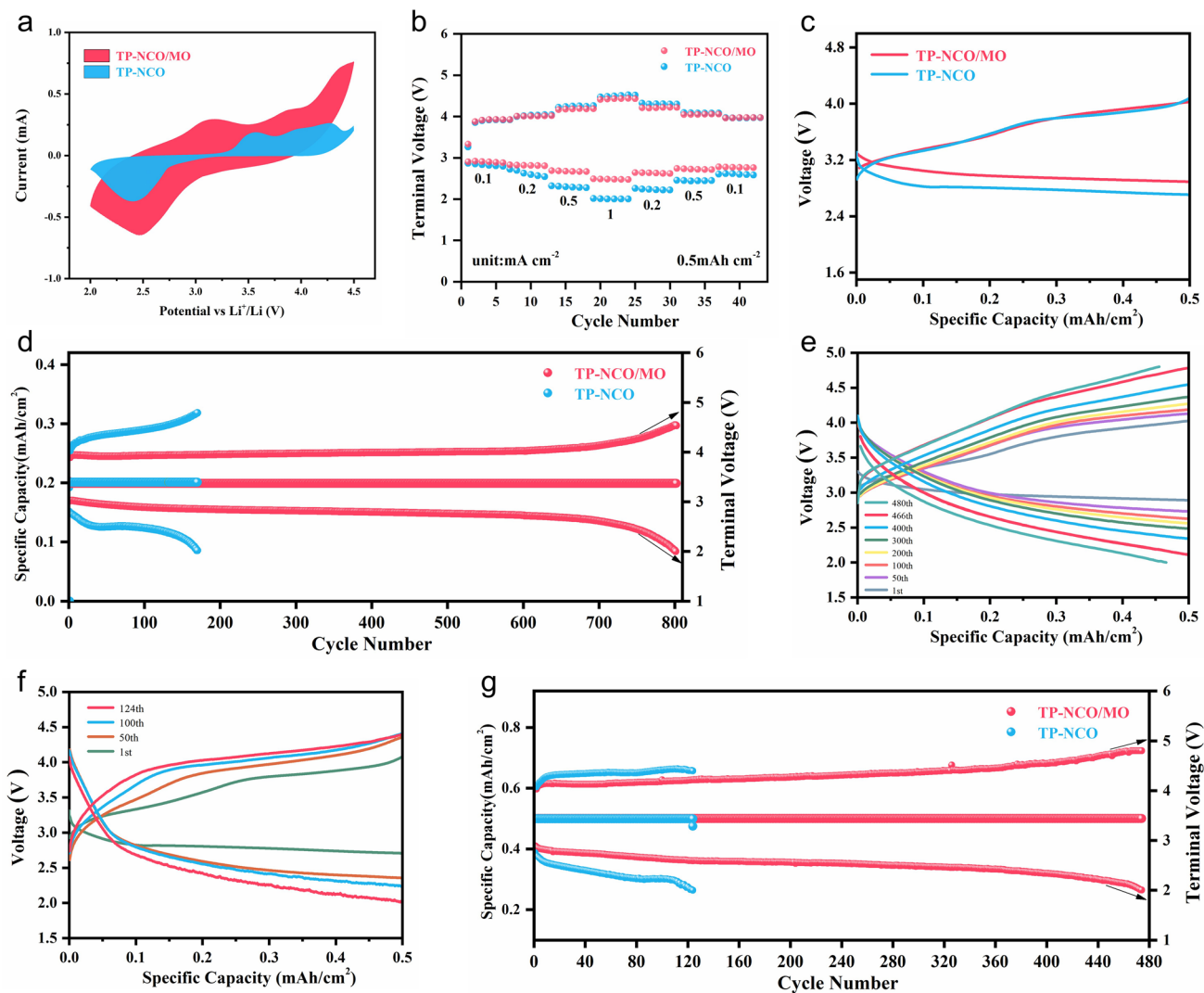
Fig. 3 **a** CV curves of TP-NCO/MO and TP-NCO cathodes recorded at a sweep rate of 0.1 mV s^{-1}. **b** Rate capability of TP-NCO/MO and TP-NCO cathodes at a fixed capacity of 0.5 mAh cm^{-2}. **c** Voltage–capacity curves for the first cycle of TP-NCO/MO and TP-NCO cathodes at a current density of 0.5 mA cm^{-2}. **d** Cycle performance of TP-NCO/MO and TP-NCO cathodes at 0.2 mA cm^{-2}. The voltage–capacity curves of **e** TP-NCO/MO and **f** TP-NCO cathodes at a current density of 0.5 mA cm^{-2} with different number of cycles. **g** Variation of termination voltage as a function of cycle number of TP-NCO/MO and TP-NCO cathodes at a current density of 0.5 mA cm^{-2}

However, for the TP-NCO cathode, when the current density restores to 0.1 mA cm^{-2}, the charging voltage of the TP-NCO cathode increases by 0.46 V and the discharge termination voltage decreases by 0.28 V. The charge/discharge overpotential is also evaluated at 0.5 mA cm^{-2}, and TP-NCO/MO and TP-NCO exhibit voltage gaps of 0.73 and 0.93 V, respectively (Fig. 3c). These results indicate that the NiCo$_2$O$_4$/MnO$_2$ Mott–Schottky heterostructure significantly enhances ORR/OER kinetics, and the effect is mainly attributed to the dual role of MnO$_2$ as an additional

active site and electron rearrangement at the heterointerface. The changes in discharge/charge termination voltage during the cycle at 0.2 mA cm^{-2} are presented in Fig. 3d. For TP-NCO/MO, the termination voltage of charge and discharge is very stable during the first 700 cycles. In contrast, when TP-NCO was used as the cathode catalyst, the charging and discharging polarization gradually increased during the cycling process, and the discharge termination voltage dropped to a lower value after 170 cycles, which may be caused by the failure of timely decomposition and continuous accumulation of discharge products.
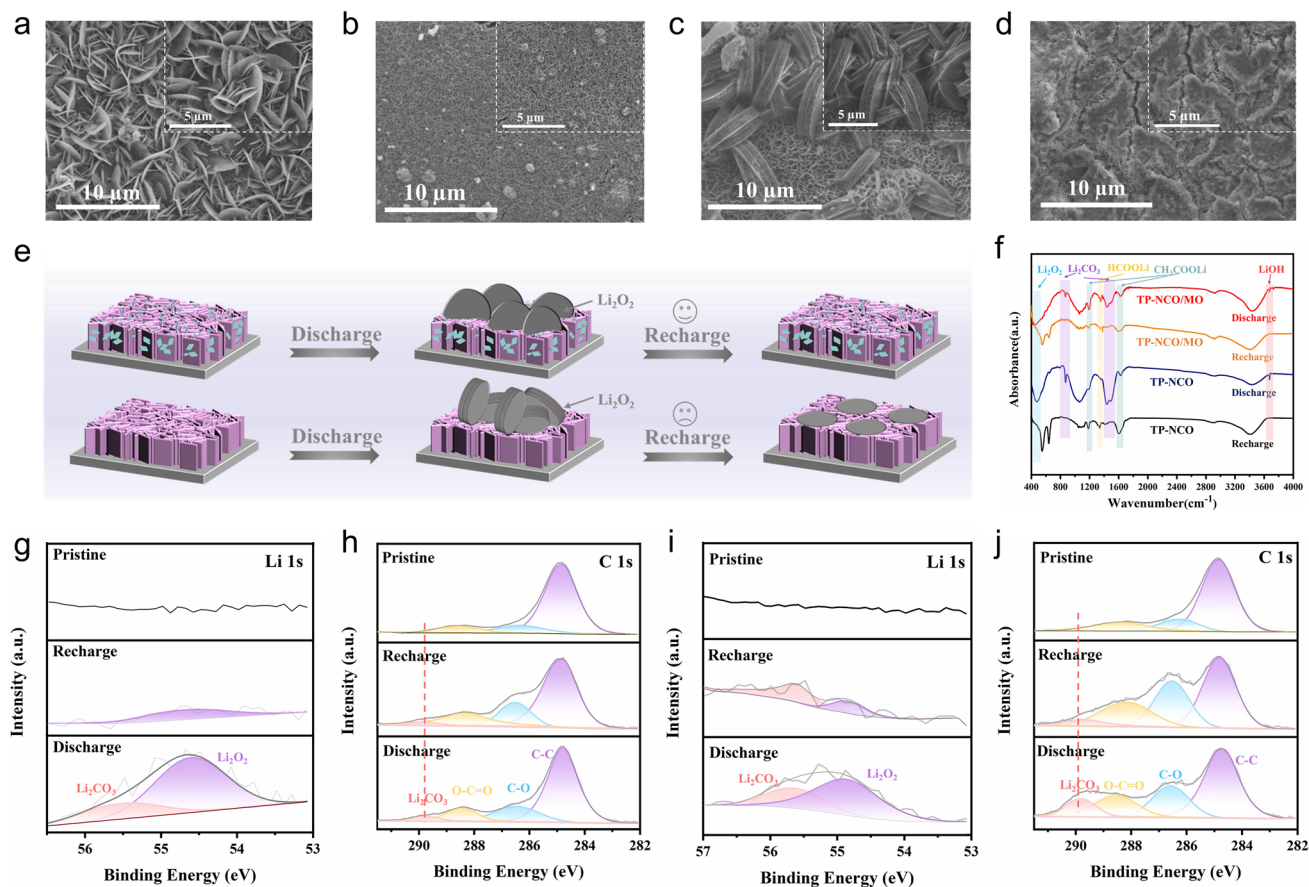
Fig. 4 SEM images of TP-NCO/MO electrode at 0.2 mA cm^{-2} **a** after deep discharge and **b** recharge. SEM images of TP-NCO electrode at 0.2 mA cm^{-2} **c** after deep discharge and **d** recharge (further enlarged in the upper right corner). **e** Illustration of the discharge–recharge process of the TP-NCO/MO and TP-NCO cathodes. **f** FTIR spectra of TP-NCO/MO and TP-NCO electrodes in the discharge and recharge states. XPS fine spectra of **g** Li 1s and **h** C 1s in the initial, discharge and recharge states of TP-NCO/MO cathode at fixed capacity of 0.2 mAh cm^{-2} and current density of 0.2 mA cm^{-2} after 20 cycles. XPS fine spectra of **i** Li 1s and **j** C 1s under the same conditions for TP-NCO cathode

Figure S18 illustrates the voltage–capacity curves of the two samples under the deep discharge at 0.2 mA cm^{-2}. The discharge capacity of TP-NCO/MO was 6.02 mAh cm^{-2}, while that of TP-NCO was only 4.34 mAh cm^{-2}. It is well known that larger current densities and larger cutoff capacities in LOBs require higher electrocatalytic activity of the catalyst materials on the cathode side [46]. The cycling performance of the two materials was further assessed at a restricted capacity of 0.5 mAh cm^{-2} and a high current density of 0.5 mA cm^{-2}. The discharge/charge curves of TP-NCO/MO and TP-NCO materials at different cycle times are shown in Fig. 3e, f. As shown in Fig. 3g, the TP-NCO/MO catalyst material can stably cycle for nearly 480 cycles at such a high current density, whereas the TP-NCO can only last for 124 cycles. Compared with

other similar catalysts that have been reported, the materials prepared in this work have a significant advantage in terms of cycling life (Fig. S20 and Table S1).

3.4 Reversibility Studies of Discharge Products

The morphology of the discharge products and the reversibility of the formation/decomposition were investigated using numerous characterization methods, such as SEM, XRD, XPS, FTIR, TEM, in situ EIS, and TOF–SIMs to understand the reaction mechanism within the TP-NCO/MO cathode. Figure 4a-d show the morphology of the TP-NCO/MO and TP-NCO surfaces in the full discharge and charge state at 0.2 mA cm^{-2}, respectively. The insets provide

enlarged views for better observation. For the TP-NCO/MO catalyst, after full discharge (Fig. 4a), it can be observed that a large "chip-like" discharge product is embedded within the nanosheet arrays, with a thickness of nearly 40 nm. The lower ends of the slice are in close contact with the $NiCo_2O_4/MnO_2$ nanosheet arrays, which means that there are sufficient contact sites between the catalyst material and the discharge product, allowing for faster and more efficient decomposition, thus reducing overpotential and enhancing the rate performance of LOBs [28]. Adequate contact between the discharge product and the cathode is a crucial factor in achieving excellent electrochemical performance. However, the actual decomposition capability also depends on the interfacial properties between the electrolyte and the discharge product, as well as between the catalyst and the discharge product. Unsurprisingly, after recharge (Fig. 4b), the "chip-like" discharge products almost decompose and disappear, and the $NiCo_2O_4/MnO_2$ nanosheet arrays are completely exposed. In sharp contrast, after the TP-NCO cathode material was completely discharged (Fig. 4c), "thousand-layer cookie-like " discharge products are observed at the top of the $NiCo_2O_4$ nanosheet arrays, with few contact sites with the electrode surface, which made subsequent fully reversible decomposition difficult, resulting in a large overpotential. It is noteworthy that the small MnO_2 sheets distributed on the surface of $NiCo_2O_4$ nanosheets of TP-NCO/MO material can provide the initial nucleation site for the deposition of the discharge products, allowing the "chip-like" discharge products to be embedded and grown in the nanosheet arrays. After recharge (Fig. 4d), some residues of the "thousand-layer cookie-like" discharge products remain on top of the TP-NCO nanosheet arrays, implying poor reversibility. Based on the above results, a schematic diagram of the formation and decomposition of discharge products in TP-NCO/MO and TP-NCO cathodes can be presented (Fig. 4e). XRD test results of TP-NCO/MO at both discharge and recharge stages suggest that the formation and decomposition of Li_2O_2 are well reversible (Fig. S23) [28]. To further investigate the changes of all the discharge products of TP-NCO/MO and TP-NCO catalyst materials during discharge and recharge, the Fourier transform infrared (FTIR) spectra of the two catalysts were tested at 0.2 mA cm^{-2} at the full discharge and recharge stages (Fig. 4f), which provides strong evidence for the types and changes of discharge products after discharge and recharge. For TP-NCO/MO catalyst materials, Li_2O_2 (472 cm^{-1}),

Li_2CO_3 (860, 1437, and 1510 cm^{-1}), HCOOLi (1360 cm^{-1}), CH_3COOLi (1197 and 1615 cm^{-1}) and LiOH (3675 cm^{-1}) were detected in the discharged state. After recharge, Li_2O_2, Li_2CO_3 and LiOH decomposed and disappeared, while HCOOLi and CH_3COOLi showed little change. For TP-NCO catalyst materials, the same discharge products were detected. However, after recharge, the results showed that the by-products CH_3COOLi and HCOOLi not only did not decompose, but also accumulated further. In contrast, TP-NCO/MO accumulated much less by-products during the cycling process, which was attributed to its lower charging voltage, reducing the occurrence of electrolyte decomposition and other side reactions caused by high potential [47]. In addition, the products of the discharge and recharge stages were further characterized by XPS (Fig. 4g-j). For the TP-NCO/MO cathode (Fig. 4g, h), the peaks fitted at 54.8 and 55.6 eV in the Li 1s fine spectrum at the discharge stage are related to Li_2O_2 and Li_2CO_3, respectively, and the corresponding peaks at 289.8 eV in the C 1s fine spectrum correspond to Li_2CO_3, which is almost completely decomposed after recharge. In contrast, in the TP-NCO cathode (Fig. 4i, j), both Li 1s and C 1s fine spectra were fitted to obtain a larger area of peaks for the by-product Li_2CO_3, which was not effectively decomposed after recharge.

The ex situ XPS and FTIR results of the discharge–recharge process further provide evidences for the high reversibility of the discharge products. Discharge and charge with unlimited capacity were performed at 0.2 mA cm^{-2}, during which 6 voltages were intercepted for XPS and FTIR characterization in this process, as shown in Fig. 5a-d. The XPS C 1s fine spectrum results show that the peak area corresponding to Li_2CO_3 at 289.8 eV gradually increases during the discharge process and then gradually decreases after charging until it disappears at stage 6 (Fig. 5b). For the XPS Li 1s fine spectrum (Fig. 5c), in stage 1, the peaks at 55.1 and 56.1 eV correlate to Li_2O_2 and Li-deficient phase $Li_{2-x}O_2$, respectively. The formation/decomposition of Li_2O_2 can induce the generation of $Li_{2-x}O_2$ [48, 49]. Further discharge to stages 2 and 3 results in the formation of crystalline Li_2O_2 as the main product. In addition, a peak belonging to Li_2CO_3 appears at stage 3 and the FTIR characterization shows the same result (Fig. 5d). In the process of recharge, Gaussian fitted peaks of Li_2O_2 and the Li-deficient phase $Li_{2-x}O_2$ appeared at stages 4, 5, and 6. Differently, the peak area ratios of Li_2O_2 and $Li_{2-x}O_2$ gradually decrease with the recharging, indicating the gradual
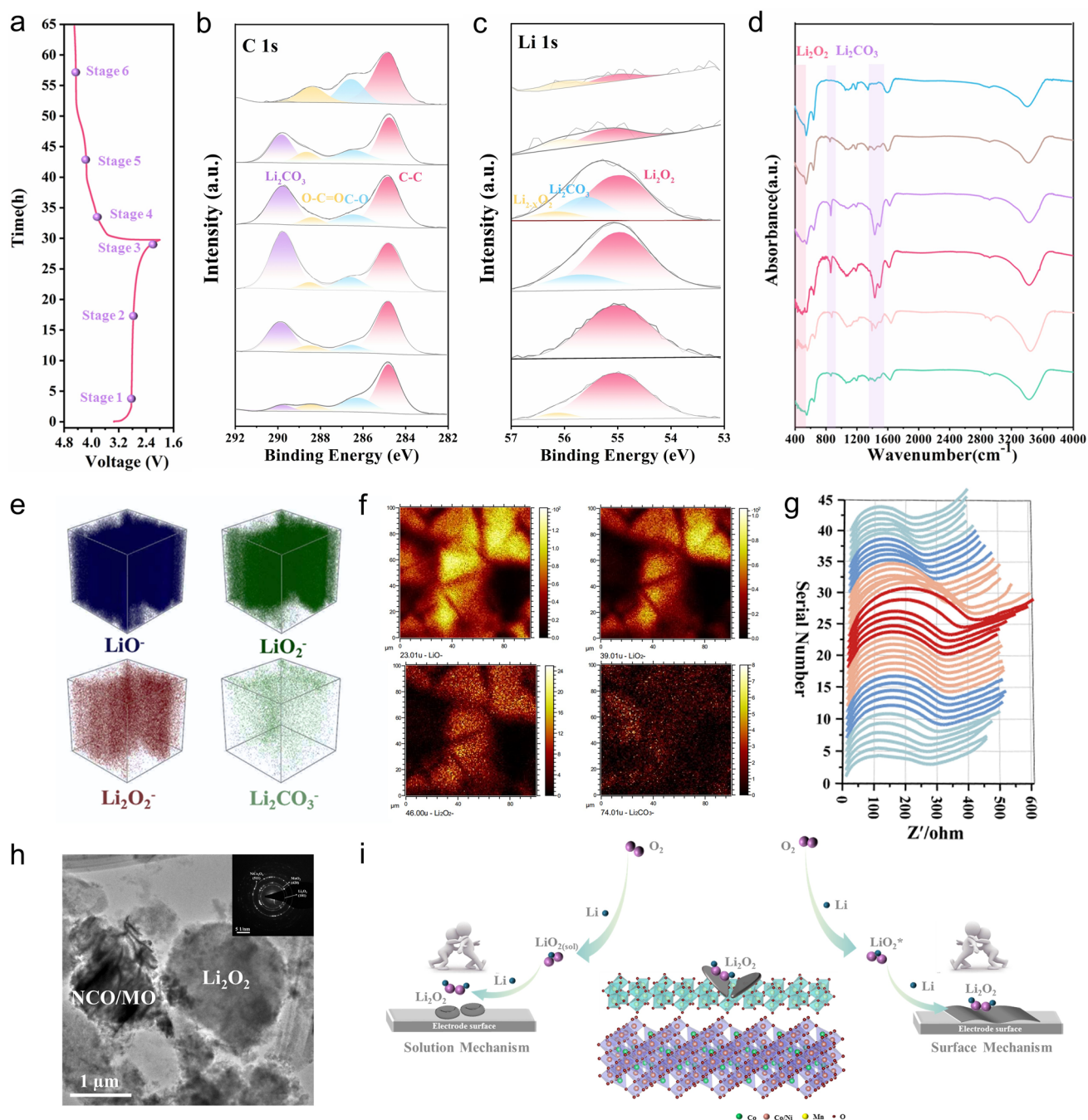
Fig. 5 **a** Discharge/charge curve of TP-NCO/MO electrode at 0.2 mA cm^{-2}. XPS fine spectra of **b** C 1s and **c** Li 1s and **d** FTIR spectra corresponding to stages (1−6). **e** 3D depth image and **f** the cross-sectional image of LiO$^-$, LiO$_2^-$, Li$_2$O$_2^-$, and Li$_2$CO$_3^-$. **g** In situ EIS spectrum of TP-NCO/MO. **h** TEM of NCO/MO cathode after deep discharge at 0.2 mA cm^{-2} (SAED in insert). **i** Schematic reaction mechanism of TP-NCO/MO

oxidation of Li$_2$O$_2$ to Li$_{2-x}$O$_2$ and subsequent decomposition. In addition, the peak corresponding to Li$_2$CO$_3$ remains visible in stage 4, but then disappears, suggesting that the by-products generated during discharge and recharge can also be decomposed in time to a certain extent, which is also confirmed by the corresponding FTIR characterization results.

To further analyze the composition and distribution of the discharge products, a TOF–SIMS analysis was performed on the TP-NCO/MO discharged electrode. LiO^-, LiO_2^-, $Li_2O_2^-$, and weak $Li_2CO_3^-$ signals were detected in selected regions (Figs. S24 and 5e, f). The results demonstrate that the discharge product primarily consisted of non-stoichiometric $Li_{2-x}O_2$ [50], which is uniformly distributed throughout the three-dimensional space. Even under unlimited discharge conditions, the amount of by-product Li_2CO_3 remains low, which is consistent with the expected reaction that may occur during the discharge stage. The in situ EIS spectrum of TP-NCO/MO was used to monitor the evolution of electrochemical impedance during charging and discharging of LOBs (Fig. 5g). Discharge and charge were conducted for 2 h at 0.2 mA cm^{-2}, and 40 sets of EIS spectra were recorded. The results of the equivalent circuit fitting of the representative 10 sets of data are shown in Table S4. In the initial state, two semicircles appear in the mid-frequency region of the EIS spectra. This may be due to the fact that the interface is not fully stabilized at the initial stage, resulting in the appearance of additional semicircles [51, 52]. During the subsequent discharge, it was replaced by a semicircle of increasing diameter, and the charge transfer impedance R_{ct} increased from 199.8 to 313 Ω, indicating the gradual accumulation of discharge products. At the end of charging, the discharge products are decomposed, and the charge transfer impedance R_{ct} gradually decreases to 208.7 Ω. After discharge, "chip-like" Li_2O_2 were further observed by TEM (Fig. 5h). Selective area electron diffraction (SAED) results confirmed the existence of $NiCo_2O_4$, MnO_2, and Li_2O_2. According to the above experimental results, the possible formation mechanism of Li_2O_2 during the discharge processes of TP-NCO/MO is shown in Fig. 5i. Based on previous reports [24, 53], the morphology of Li_2O_2 formed during the discharge process is determined by the adsorption free energy on the electrode surface of the intermediate and the dissolution free energy of the electrolyte. It can be found that the TP-NCO/MO heterostructure materials obtained chip-like Li_2O_2 embedded nanosheet arrays under the competition of surface and solution mechanisms. This cross-embedded arrangement not only provides abundant contact sites with the electrode but also prevents passivation of the electrode.

3.5 Theoretical Insights into Superior Performance

DFT calculations have been employed to unravel the underlying mechanisms through which heterostructures comprising $NiCo_2O_4$ and MnO_2 can enhance the catalytic performance in LOBs. Detailed modeling specifics can be found in Fig. S28. In Fig. 6a, the partial density of states (PDOS) of $NiCo_2O_4$ and $NiCo_2O_4/MnO_2$ have been computed, revealing that both systems exhibit metallic characteristics, with the density of states at the Fermi level (E_f) primarily governed by O-2p and Co-3d orbitals. It is noteworthy that $NiCo_2O_4/MnO_2$ exhibits a greater electron density in the vicinity of E_f compared to $NiCo_2O_4$. This increased electron density stems mainly from the contributions of Mn-3d and O-2p orbitals in MnO_2. It is suggested that the assembly of $NiCo_2O_4$ and MnO_2 heterostructures can significantly enhance the conductivity of the catalyst materials. Such enhancement is highly advantageous for promoting the three-phase reaction at the cathode-side interface. The illustration in Fig. 6a effectively portrays the charge density surrounding the Fermi level of $NiCo_2O_4$ and $NiCo_2O_4/MnO_2$. By examining the image, it becomes evident that the density of states primarily originates from the Co and O atoms for $NiCo_2O_4$, while for $NiCo_2O_4/MnO_2$, it is primarily contributed by Co, Mn, and O atoms at the surface. Figure 6b demonstrates the charge redistribution occurring at the $NiCo_2O_4/MnO_2$ heterogeneous interface through the charge density difference (CDD). At the interface of $NiCo_2O_2@MnO_2$ heterojunction, a series of interface interactions will occur due to the differences in crystal structure and electronic state of the two materials. Specifically, the Mn atoms in MnO_2 tend to lose some electrons to form positively charged ions (Mn^{3+} or Mn^{4+}). Meanwhile, the oxygen atoms on the surface of $NiCo_2O_2$ tend to gain these electrons, forming negatively charged ions (O^{2-}). This charge redistribution leads to strong electrostatic interactions at the interface, resulting in a stable heterojunction structure. The exquisite lattice compatibility between $NiCo_2O_4$ and MnO_2 gives rise to undulating and uninterrupted electric field variations at the interface. This phenomenon, coupled with the contrasting wave amplitudes exhibited by $NiCo_2O_4$ and MnO_2, exerts a profound influence on managing the charge transfer process during the adsorption of intermediates while ensuring the remarkable stability of the interface by preserving its high level of structural integrity. The work function of both $NiCo_2O_4$ and $NiCo_2O_4/MnO_2$ which reflects the rate of reaction kinetics

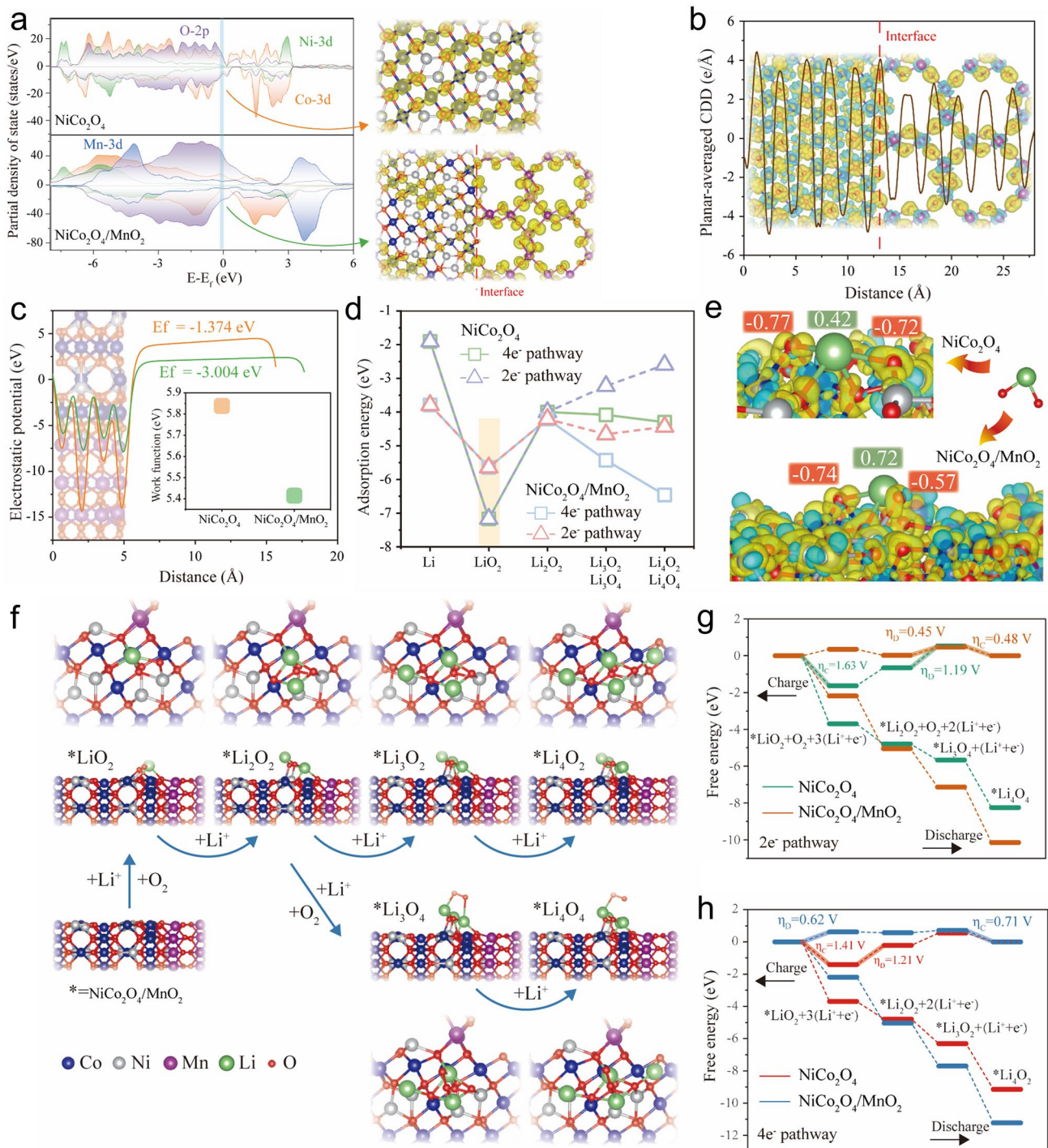**Fig. 6** **a** Partial density of states of $NiCo_2O_4$ and $NiCo_2O_4/MnO_2$, respectively. The diagrams are the charge densities near the Fermi energy level. **b** Planar-averaged charge density difference (CDD) across the z-direction for the $NiCo_2O_4/MnO_2$ heterostructure. **c** Plot of the electrostatic potential along the $NiCo_2O_4/MnO_2$ slab model. The inset is the work function of $NiCo_2O_4$ and $NiCo_2O_4/MnO_2$. **d** Adsorption energy of the discharge intermediates for $4e^-$ pathway and $2e^-$ pathway, respectively. **e** CDD and Bader charge for the LiO_2 adsorbed at $NiCo_2O_4$, $NiCo_2O_4/MnO_2$. **f** Atomic configurations of the possible reaction paths of Li^+ and O_2 on the surface of $NiCo_2O_4/MnO_2$. Free energy diagrams of the **g** $2e^-$ pathway and **h** $4e^-$ pathway for the discharge and charge process on the $NiCo_2O_4$ and $NiCo_2O_4/MnO_2$

of the surface was calculated as depicted in Fig. 6c. The values for $NiCo_2O_4$ and $NiCo_2O_4/MnO_2$ are measured to be 5.84 and 5.42 eV, respectively. Remarkably, the lower work function of $NiCo_2O_4/MnO_2$ suggests a higher level of reactivity at the heterogeneous interface formed by MnO_2. This result aligns with the experimental observation that the catalytic performance of $NiCo_2O_4/MnO_2$ heterogeneous structure surpasses that of its counterpart, the $NiCo_2O_4$ homogeneous structure.

The adsorption energies of discharge/charge intermediates under two-electron and four-electron reaction pathways for $NiCo_2O_4/MnO_2$ and $NiCo_2O_4$ are calculated in Fig. 6d. Specifically, the adsorption energy of $NiCo_2O_4/MnO_2$ and $NiCo_2O_4$ on Li and the intermediate LiO_2 are consistent under the two pathways. Notably, the adsorption energy of $NiCo_2O_4/MnO_2$ on Li is stronger than that of $NiCo_2O_4$, and intriguingly, the adsorption of $NiCo_2O_4/MnO_2$ on the intermediate product LiO_2 is weaker compared to $NiCo_2O_4$. The diagram of CDD and Bader charge of LiO_2 adsorbed on the surface of $NiCo_2O_4$ and $NiCo_2O_4/MnO_2$ in Fig. 6e demonstrate that Li loses more electrons, while O receives fewer electrons after the construction of the heterostructures, which is the reason behind the weaker adsorption of LiO_2 on $NiCo_2O_4/MnO_2$. More electrons lost by Li may be transferred to the substrate MnO_2, as analyzed in Fig. 6b. The weak adsorption of the intermediate product LiO_2 within an optimal range facilitates the swift conversion of the intermediate to the final product. Consequently, this accelerates the kinetics of discharge product formation. Furthermore, this appropriate adsorption of LiO_2 allows the discharge product to strike a balance between surface-mediated and solution-mediated mechanisms. As a result, it assumes a chip-like morphology that is embedded, possesses high capacity, and offers more contact sites with the catalyst substrate, ultimately leading to highly reversible and high-capacity LOBs. Moreover, as adsorption progresses, $NiCo_2O_4/MnO_2$ demonstrates stronger adsorption energy than $NiCo_2O_4$. Among these observations, the adsorption is particularly potent along the four-electron pathway. However, the adsorption energy of different intermediates within the four-electron pathway exhibits significant variation, thereby resulting in a larger overpotential. Further analysis on this matter will be explored in subsequent discussions. Figure 6f presents the schematic diagram depicting the reaction route at each step in the discharge process on the surface of $NiCo_2O_4/MnO_2$. The corresponding redox free energies of $NiCo_2O_4$ and

$NiCo_2O_4/MnO_2$ following the four-electron pathway and the two-electron pathway at each step are exhibited in Fig. 6g, h. In the two-electron path (Fig. 6g), $NiCo_2O_4$ exhibits a maximum overpotential η_D of 1.19 V, whereas $NiCo_2O_4/MnO_2$ demonstrates a significantly lower η_D of only 0.45 V. On the contrary, during the charge process, $NiCo_2O_4$ displays an overpotential η_C of 1.63 V, while $NiCo_2O_4/MnO_2$ exhibits a much lower η_C of only 0.48 V. These observations indicate that $NiCo_2O_4/MnO_2$ possesses a lower overpotential in the discharge/charge process, which is in alignment with the prior battery test results. Similar trends are highlighted in the four-electron path (Fig. 6h). The discharge and charge overpotentials η_D/η_C of $NiCo_2O_4$ and $NiCo_2O_4/MnO_2$ are 1.21/1.41 and 0.62/0.71 V, respectively, with both $NiCo_2O_4/MnO_2$ exhibiting lower overpotentials. Moreover, our findings reveal that the discharge/charge overpotential of the four-electron path for the $NiCo_2O_4/MnO_2$ catalyst is higher than that of the two-electron path, which concurs with the results depicted in Fig. 6d, further supporting the notion that the catalytic process is more favorable through the two-electron pathway, consistent with experimental results. These calculation results illustrate that constructing effective heterostructures is a crucial strategy in designing high-efficiency electrocatalysts for LOBs.

4 Conclusions

In summary, self-supporting $NiCo_2O_4/MnO_2$ with a Mott–Schottky heterogeneous structure was successfully prepared on titanium paper (TP-NCO/MO). The construction of the NCO/MO Mott–Schottky heterostructure triggers the interface disturbance and changes in the energy band structure to fundamentally optimize the adsorption of reaction intermediates, refine the morphology of the discharge products, and enhance the efficiency of the generation and dissolution of the discharge products. In addition, MnO_2 serves as an effective active site in OER and ORR, and by providing additional reaction sites, MnO_2 contributes to the acceleration of the reaction rate and the decrease of the overpotential, thus enhancing the catalytic activity. DFT calculations were used to understand how the NCO/MO heterostructures enhance the dynamics of ORR and OER in LOBs. The assembly of this heterostructure enhances the electrical conductivity of the catalyst materials, resulting in a more efficient three-phase reaction at the cathode interface. The

lattice compatibility between $NiCo_2O_4$ and MnO_2 creates undulating electric field variations at the interface, which, combined with their contrasting wave amplitudes, influences the charge transfer process during the adsorption of intermediates and maintains the structural integrity of the interface. As a result, TP-NCO/MO as a cathode catalyst for LOB exhibits excellent catalytic activity. This work regulates the morphology of discharge products by constructing Mott–Schottky heterostructures using a facile method, providing reference significance for designing efficient catalysts to optimize the adsorption of reaction intermediates.

Declarations

Supplementary Information The online version contains supplementary material available at https://doi.org/10.1007/s40820-024-01476-4.

References

1. M. Asadi, B. Sayahpour, P. Abbasi, A.T. Ngo, K. Karis et al., A lithium–oxygen battery with a long cycle life in an air-like atmosphere. Nature **555**, 502–506 (2018). https://doi.org/10.1038/nature25984

2. Y. Wang, Y. Zhang, G. Gao, Y. Fan, R. Wang et al., Effectively modulating oxygen vacancies in flower-like δ-MnO_2 nanostructures for large capacity and high-rate zinc-ion storage. Nano-Micro Lett. **15**, 219 (2023). https://doi.org/10.1007/s40820-023-01194-3

3. A. Hu, W. Chen, X. Du, Y. Hu, T. Lei et al., An artificial hybrid interphase for an ultrahigh-rate and practical lithium metal anode. Energy Environ. Sci. **14**, 4115–4124 (2021). https://doi.org/10.1039/d1ee00508a

4. J. Lu, L. Li, J.-B. Park, Y.-K. Sun, F. Wu et al., Aprotic and aqueous Li–O_2 batteries. Chem. Rev. **114**, 5611–5640 (2014). https://doi.org/10.1021/cr400573b

5. Z.-L. Wang, D. Xu, J.-J. Xu, X.-B. Zhang, Oxygen electrocatalysts in metal–air batteries: from aqueous to nonaqueous electrolytes. Chem. Soc. Rev. **43**, 7746–7786 (2014). https://doi.org/10.1039/C3CS60248F

6. J. Lai, Y. Xing, N. Chen, L. Li, F. Wu et al., Electrolytes for rechargeable lithium–air batteries. Angew. Chem. Int. Ed. **59**, 2974–2997 (2020). https://doi.org/10.1002/anie.201903459

7. J. Liu, Y. Zhao, X. Li, C. Wang, Y. Zeng et al., $CuCr_2O_4$@rGO nanocomposites as high-performance cathode catalyst for rechargeable lithium–oxygen batteries. Nano-Micro Lett. **10**, 22 (2017). https://doi.org/10.1007/s40820-017-0175-z

8. C. Zhao, Z. Yan, B. Zhou, Y. Pan, A. Hu et al., Identifying the role of lewis-base sites for the chemistry in lithium-oxygen batteries. Angew. Chem. Int. Ed. **62**, e202302746 (2023). https://doi.org/10.1002/anie.202302746

9. G. Yue, Z. Hong, Y. Xia, T. Yang, Y. Wu, Bifunctional electrocatalysts materials for non-aqueous Li–air batteries. Coatings **12**, 1227 (2022). https://doi.org/10.3390/coatings12081227

10. Y. Dou, S. Xing, Z. Zhang, Z. Zhou, Solving the singlet oxygen puzzle in metal-O_2 batteries: current progress and future directions. Electrochem. Energy Rev. **7**, 6 (2024). https://doi.org/10.1007/s41918-023-00201-w

11. R. Li, A. Hu, C. Zhao, B. Zhou, M. He et al., Tailoring mixed geometrical configurations in amorphous catalysts to activate oxygen electrode reactions of lithium-oxygen batteries. Chem. Eng. J. **452**, 139162 (2023). https://doi.org/10.1016/j.cej.2022.139162

12. J. Lu, Y. Lei, K.C. Lau, X. Luo, P. Du et al., A nanostructured cathode architecture for low charge overpotential in lithium-oxygen batteries. Nat. Commun. **4**, 2383 (2013). https://doi.org/10.1038/ncomms3383

13. J.-J. Xu, Z.-L. Wang, D. Xu, L.-L. Zhang, X.-B. Zhang, Tailoring deposition and morphology of discharge products towards high-rate and long-life lithium-oxygen batteries. Nat. Commun. **4**, 2438 (2013). https://doi.org/10.1038/ncomms3438

14. L.-N. Song, W. Zhang, Y. Wang, X. Ge, L.-C. Zou et al., Tuning lithium-peroxide formation and decomposition routes with single-atom catalysts for lithium-oxygen batteries. Nat. Commun. **11**, 2191 (2020). https://doi.org/10.1038/s41467-020-15712-z

15. X. Li, Z. Qiang, G. Han, S. Guan, Y. Zhao et al., Enhanced redox electrocatalysis in high-entropy perovskite fluorides by tailoring d-p hybridization. Nano-Micro Lett. **16**, 55 (2023). https://doi.org/10.1007/s40820-023-01275-3

16. C. Zhang, R. Du, J.J. Biendicho, M. Yi, K. Xiao et al., Tubular CoFeP@CN as a Mott-Schottky catalyst with multiple adsorption sites for robust lithium–sulfur batteries. Adv. Energy Mater. **11**, 2100432 (2021). https://doi.org/10.1002/aenm.202100432

17. X. Zhao, M. Liu, Y. Wang, Y. Xiong, P. Yang et al., Designing a built-In electric field for efficient energy electrocatalysis. ACS Nano **16**, 19959–19979 (2022). https://doi.org/10.1021/acsnano.2c09888

18. C. Wu, G. Qi, J. Zhang, J. Cheng, B. Wang, Porous Mo_3 P/Mo nanorods as efficient Mott-Schottky cathode catalysts for low polarization Li-CO_2 battery. Small **19**, e2302078 (2023). https://doi.org/10.1002/smll.202302078

19. Y. Xia, T. Yang, Z. Wang, T. Mao, Z. Hong et al., Van der waals forces between S and P ions at the CoP-$C@MoS_2$/C heterointerface with enhanced lithium/sodium storage. Adv. Funct. Mater. **33**, 2302830 (2023). https://doi.org/10.1002/adfm.202302830

20. M. Shi, Z. Liu, S. Zhang, S. Liang, Y. Jiang et al., A Mott-Schottky heterogeneous layer for Li–S batteries: enabling both high stability and commercial-sulfur utilization. Adv. Energy Mater. **12**, 2103657 (2022). https://doi.org/10.1002/aenm.202103657

21. A. Hu, M. Zhou, T. Lei, Y. Hu, X. Du et al., Optimizing redox reactions in aprotic lithium–sulfur batteries. Adv. Energy Mater. **10**, 2002180 (2020). https://doi.org/10.1002/aenm.202002180

22. J. Hong, L. Zhang, Q. Zhu, Z. Du, Y. Zhou et al., A macroporous carbon nanoframe for hosting Mott-Schottky Fe-Co/Mo_2C sites as an outstanding bi-functional oxygen electrocatalyst. Mater. Horiz. **10**, 5969–5982 (2023). https://doi.org/10.1039/d3mh01237a

23. X. Zhao, J. Chen, Z. Bi, S. Chen, L. Feng et al., Electron modulation and morphology engineering jointly accelerate oxygen reaction to enhance Zn-air battery performance. Adv. Sci. **10**, e2205889 (2023). https://doi.org/10.1002/advs.202205889

24. L. Johnson, C. Li, Z. Liu, Y. Chen, S.A. Freunberger et al., The role of LiO_2 solubility in O_2 reduction in aprotic solvents and its consequences for Li–O_2 batteries. Nat. Chem. **6**, 1091–1099 (2014). https://doi.org/10.1038/nchem.2101

25. Y. Wang, N.-C. Lai, Y.-R. Lu, Y. Zhou, C.-L. Dong et al., A solvent-controlled oxidation mechanism of Li_2O_2 in lithium-oxygen batteries. Joule **2**, 2364–2380 (2018). https://doi.org/10.1016/j.joule.2018.07.021

26. Q. Xia, D. Li, L. Zhao, J. Wang, Y. Long et al., Recent advances in heterostructured cathodic electrocatalysts for non-aqueous Li–O_2 batteries. Chem. Sci. **13**, 2841–2856 (2021). https://doi.org/10.1039/d1sc05781b

27. P. Wang, C. Li, S. Dong, X. Ge, P. Zhang et al., Hierarchical $NiCo_2S_4$@NiO core–shell heterostructures as catalytic cathode for long-life Li–O_2 batteries. Adv. Energy Mater. **9**, 1900788 (2019). https://doi.org/10.1002/aenm.201900788

28. P. Zhang, S. Zhang, M. He, J. Lang, A. Ren et al., Realizing the embedded growth of large Li_2O_2 aggregations by matching different metal oxides for high-capacity and high-rate lithium oxygen batteries. Adv. Sci. **4**, 1700172 (2017). https://doi.org/10.1002/advs.201700172

29. J. Hafner, Materials simulations using VASP—a quantum perspective to materials science. Comput. Phys. Commun. **177**, 6–13 (2007). https://doi.org/10.1016/j.cpc.2007.02.045

30. G. Kresse, J. Furthmüller, Efficient iterative schemes for *ab initio* total-energy calculations using a plane-wave basis set. Phys. Rev. B Condens. Matter **54**, 11169–11186 (1996). https://doi.org/10.1103/physrevb.54.11169

31. S. Grimme, S. Ehrlich, L. Goerigk, Effect of the damping function in dispersion corrected density functional theory. J. Comput. Chem. **32**, 1456–1465 (2011). https://doi.org/10.1002/jcc.21759

32. S.L. Dudarev, G.A. Botton, S.Y. Savrasov, C.J. Humphreys, A.P. Sutton, Electron-energy-loss spectra and the structural stability of nickel oxide: An LSDA+U study. Phys. Rev. B **57**, 1505–1509 (1998). https://doi.org/10.1103/physrevb.57.1505

33. M. Cococcioni, S. de Gironcoli, Linear response approach to the calculation of the effective interaction parameters in the LDA+U method. Phys. Rev. B **71**, 035105 (2005). https://doi.org/10.1103/physrevb.71.035105

34. Y. Zheng, K. Song, J. Jung, C. Li, Y.-U. Heo et al., Critical descriptor for the rational design of oxide-based catalysts in rechargeable Li–O_2 batteries: surface oxygen density. Chem. Mater. **27**, 3243–3249 (2015). https://doi.org/10.1021/acs.chemmater.5b00056

35. Y.-F. Xu, Y. Chen, G.-L. Xu, X.-R. Zhang, Z. Chen et al., RuO_2 nanoparticles supported on MnO_2 nanorods as high efficient bifunctional electrocatalyst of lithium-oxygen battery. Nano Energy **28**, 63–70 (2016). https://doi.org/10.1016/j.nanoen.2016.08.009

36. C.-H. Chen, S. Suib, Control of catalytic activity via porosity, chemical composition, and morphology of nanostructured porous manganese oxide materials. J. Chin. Chem. Soc. **59**, 465–472 (2012). https://doi.org/10.1002/jccs.201100699

37. S. Liu, Y. Zhu, J. Xie, Y. Huo, H.Y. Yang et al., Direct growth of flower-like δ-MnO_2 on three-dimensional graphene for high-performance rechargeable Li–O_2 batteries. Adv. Energy Mater. **4**, 1301960 (2014). https://doi.org/10.1002/aenm.201301960

38. X. Hu, X. Han, Y. Hu, F. Cheng, J. Chen, ε-MnO_2 nanostructures directly grown on Ni foam: a cathode catalyst for rechargeable Li–O_2 batteries. Nanoscale **6**, 3522–3525 (2014). https://doi.org/10.1039/c3nr06361e

39. B. Liu, Y. Sun, L. Liu, S. Xu, X. Yan, Advances in manganese-based oxides cathodic electrocatalysts for Li–air batteries. Adv. Funct. Mater. **28**, 1704973 (2018). https://doi.org/10.1002/adfm.201704973

40. S. Zhou, P. Huang, T. Xiong, F. Yang, H. Yang et al., Sub-thick electrodes with enhanced transport kinetics via *in situ* epitaxial heterogeneous interfaces for high areal-capacity lithium ion

batteries. Small **17**, e2100778 (2021). https://doi.org/10.1002/smll.202100778

41. Y. Yan, Z. Ran, T. Zeng, X. Wen, H. Xu et al., Interfacial electron redistribution of *Hydrangea*-like NiO@Ni$_2$P heterogeneous microspheres with dual-phase synergy for high-performance lithium-oxygen battery. Small **18**, e2106707 (2022). https://doi.org/10.1002/smll.202106707

42. S. Zhang, C. Tan, R. Yan, X. Zou, F.-L. Hu et al., Constructing built-in electric field in heterogeneous nanowire arrays for efficient overall water electrolysis. Angew. Chem. Int. Ed. **62**, e202302795 (2023). https://doi.org/10.1002/anie.202302795

43. J. Sun, Y. Chang, J. Zhang, S. Tian, X. Liu et al., Epitaxial growth of Ni$_x$Co$_{3-x}$S$_4$ nanoflakes from co-based Prussian blue analog for high-performance pseudocapacitors. Chem. Eng. J. **473**, 145175 (2023). https://doi.org/10.1016/j.cej.2023.145175

44. S.-S. Li, X.-L. Zhao, Y.-S. Liu, J.-J. Liu, K.-X. Wang et al., Tailoring the nucleation and growth routes of discharge products for lithium-oxygen batteries through the facet engineering of Ni$_2$P catalysts. Energy Storage Mater. **56**, 506–514 (2023). https://doi.org/10.1016/j.ensm.2023.01.023

45. L. Jin, A. Xing, Z. Zhu, K. Fu, M. Zhou et al., *In situ* potential-regulated architecture of an ultrafine Ru-based electrocatalyst for ultralow overpotential lithium-oxygen batteries. Chem. Commun. **59**, 5926–5929 (2023). https://doi.org/10.1039/d3cc00589e

46. T. Liu, S. Zhao, Q. Xiong, J. Yu, J. Wang et al., Reversible discharge products in Li–air batteries. Adv. Mater. **35**, 2208925 (2023). https://doi.org/10.1002/adma.202208925

47. P. Wang, Y. Ren, R. Wang, P. Zhang, M. Ding et al., Atomically dispersed cobalt catalyst anchored on nitrogen-doped carbon nanosheets for lithium-oxygen batteries. Nat. Commun. **11**, 1576 (2020). https://doi.org/10.1038/s41467-020-15416-4

48. G. Zhang, G. Li, J. Wang, H. Tong, J. Wang et al., 2D SnSe cathode catalyst featuring an efficient facet-dependent selective Li$_2$O$_2$ growth/decomposition for Li–oxygen batteries. Adv. Energy Mater. **12**, 2103910 (2022). https://doi.org/10.1002/aenm.202103910

49. T. Yang, Y. Xia, T. Mao, Q. Ding, Z. Wang et al., Phosphorus vacancies and heterojunction interface as effective lithium-peroxide promoter for long-cycle life lithium–oxygen batteries. Adv. Funct. Mater. **32**, 2209876 (2022). https://doi.org/10.1002/adfm.202209876

50. W.-L. Bai, Z. Zhang, K.-X. Wang, J.-S. Chen, Tuning discrete growth of ultrathin nonstoichiometric Li$_{2-x}$O$_2$ discs to achieve high cycling performance Li–O$_2$ battery. Battery Energy **1**, 20220019 (2022). https://doi.org/10.1002/bte2.20220019

51. D.M. Josepetti, B.P. Sousa, S.A.J. Rodrigues, R.G. Freitas, G. Doubek, The initial stages of Li$_2$O$_2$ formation during oxygen reduction reaction in Li-O$_2$ batteries: The significance of Li$_2$O$_2$ in charge-transfer reactions within devices. J. Energy Chem. **88**, 223–231 (2024). https://doi.org/10.1016/j.jechem.2023.09.034

52. I. Landa-Medrano, I. Ruiz de Larramendi, N. Ortiz-Vitoriano, R. Pinedo, J. Ignacio Ruiz de Larramendi et al., *In situ* monitoring of discharge/charge processes in Li–O$_2$ batteries by electrochemical impedance spectroscopy. J. Power Sources **249**, 110–117 (2014). https://doi.org/10.1016/j.jpowsour.2013.10.077

53. A.C. Luntz, B.D. McCloskey, Nonaqueous Li-air batteries: a status report. Chem. Rev. **114**, 11721–11750 (2014). https://doi.org/10.1021/cr500054y